Infrared microspectroscopy beamline BL06B at SSRF

Te Ji[1] · Hua-Chun Zhu[1] · Wei-Wei Peng[1] · Jie Wang[1] · Hong-Wei Zhao[1] · Ai-Guo Li[1] · Min Chen[1]

Abstract

The infrared microspectroscopy beamline (BL06B) is a phase II beamline project at the Shanghai Synchrotron Radiation Facility (SSRF). The construction and optical alignment of BL06B were completed by the end of 2020. By 2021, it became accessible to users. The synchrotron radiation infrared (SRIR) source included edge radiation (ER) and bending magnet radiation (BMR). The extracted angles in the horizontal and vertical directions were 40 and 20 mrad, respectively. The photon flux, spectral resolution, and focused spot size were measured at the BL06B endstation, and the experimental results were consistent with theoretical calculations. SRIR light has a small divergence angle, high brightness, and a wide wavelength range. As a source of IR microscopy, it can easily focus on a diffraction-limited spatial resolution with a high signal-to-noise ratio (SNR). The BL06B endstation can be applied in a wide range of research fields, including materials, chemistry, biology, geophysics, and pharmacology.

Keywords Synchrotron radiation · Infrared beamline · Infrared microspectroscopy

1 Introduction

IR spectroscopy is a powerful analytical technology because a variety of special absorption bands are relevant to molecular structures in the IR region. They are used in a wide range of fields. The synchrotron radiation infrared (SRIR) source is 100–1000 times brighter than conventional sources. SRIR sources exhibit many advantages, such as a small divergence angle, high collimation, and wide wavelength range [1, 2]. When SRIR is used as the source for the IR microscope, the spatial resolution approaches the optical diffraction limit. The fine structures of the samples are observed at the micron scale. Recently, new experimental opportunities and wide applications have been studied by scientists owing to advanced SRIR sources and detectors [3–13].

In the last twenty years, a number of SRIR beamlines have been constructed in third-generation SR facilities throughout the world [14–17]. The Shanghai Synchrotron Radiation Facility (SSRF) is a third-generation light source with an energy of 3.5 GeV and a beam current of 240 mA for daily operation. Its spectral range is from the far-infrared to the hard X-ray region [18, 19]. Currently, more than 20 beamlines are in operation at the SSRF. The dynamic Line (D-line) of the Shanghai Light Source is a phase II beamline project. The D-line includes two beamlines and three experimental endstations. One of the beamlines is the IR beamline BL06B based on a bending magnet source, and the other is the energy-dispersive X-ray absorption spectroscopy (ED-XAS) beamline, BL05U, based on an undulator source. The overall goal of the D-line is to couple the X-ray and IR light at the same point of experimental sample. It is possible to detect the dynamic processes of molecular, atomic, and electronic structures using the simultaneous acquisition mode. ED-XAS and IR spectroscopy are complementary methods for examining the different energy-level structures of the samples. In addition to the combined experiment, two different endstations can independently conduct different studies.

✉ Ai-Guo Li
liag@sari.ac.cn

✉ Min Chen
chenm@sari.ac.cn

1 Shanghai Synchrotron Radiation Facility, Shanghai Advanced Research Institute, Chinese Academy of Sciences, Shanghai 201210, China

The IR beamline BL06B is a branch of D-line. The construction of the BL06B was completed by the end of 2020. It was commissioned and opened to the users by 2021. The experimental endstation of BL06B is optimized for the mid-infrared and far-infrared regions, and it is equipped with a Fourier transform infrared (FTIR) spectrometer, an IR microscope, and a scanning near-field optical microscope (SNOM). The spatial resolution of SRIR microscope approaches the theoretical diffraction limit; therefore, the fine structure of the micron region can be detected. With IR SNOM, the spatial resolution is determined by the curvature radius of the AFM tip, which is better than 50 nm. Furthermore, IR endstation can be applied in a wide range of fields, including materials, chemistry, biology, geophysics, pharmacology, and cultural heritage.

In this study, the optical layout and endstation of the IR beamline BL06B are introduced at the SSRF. Furthermore, the experimental equipment and methods are also presented. The details of the first commissioning results are described, including the photon flux, spectral resolution, focused spot size, and primary user achievements.

2 Beamline

2.1 Light source

The SSRF is a third-generation synchrotron radiation source with an energy of 3.5 GeV and maximum current of 300 mA. In recent years, the top–up mode has been in operation for users with a beam current of 240 mA. The IR branch of the D-line is located at BL06B of the SSRF. The advantages of SSRF include low emittance and stability of the electron beam. However, the extraction ports of the bending magnet limit the extracted angle in the vertical direction. However, this method is not suitable for IR source extraction. The edge radiation (ER) is concentrated closer to the beamline axis.

It exhibits less brightness degradation owing to spherical aberrations and additional aperture restrictions in the beamline. Hence, the ER is advantageous as a bright SRIR source [20]. ER and bending magnet radiation (BMR) have been used as IR sources in several SR facilities. Both the ER and BMR are extracted from the storage ring as the IR sources of BL06B. The extracted solid angle is 40 mrad (− 15 to 25 mrad) in the horizontal direction and 20 mrad (− 10 to 10 mrad) in the vertical direction.

2.2 Extraction mirror M1

The first plane mirror, M1 (extraction mirror), is located 1.806 m from the light source, and it is used to reflect the infrared beam. Given that high-energy photons, emitted from the light source, are absorbed by plane mirror M1, the thermal load (intense X-ray and UV radiation) is excessively high. The total thermal load is calculated to reach 3000 W, and the maximum power density is 205 W/mm^2 at the mirror surface. If the extraction mirror is not treated, then it is heated to very high temperatures, resulting in significant distortion. The heat load can be removed by cutting a slot on extraction mirror M1. However, infrared photon flux is only slightly affected. A slot of 3.0 mm is an appropriate size. Detailed descriptions and calculations are provided in Ref. [1].

The dimensions of M1 are 140 mm × 70 mm × 20 mm ($L \times W \times H$), and the slot length is 110 mm. The substrate of the extraction mirror is Glidcop, which is coated with a ca. 200-nm layer of aluminum. A photon mask is placed in front of M1, and the mirror is indirectly water-cooled.

2.3 Beamline optics

An optical schematic of the IR beamline BL06B layout is shown in Fig. 1. The beamline includes 17 mirrors and slits, CVD, BPM, and other equipment. The detailed parameters

Fig. 1 (Color online) Optical layout of the SRIR beamline BL06B at SSRF
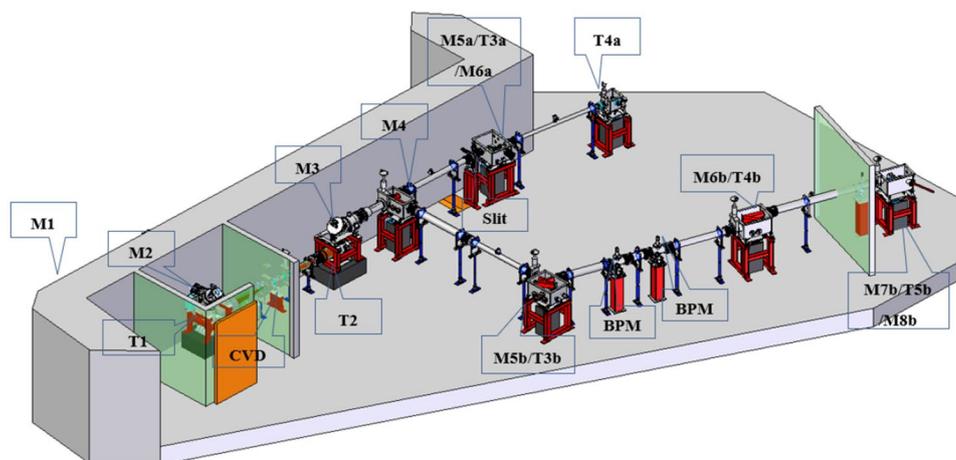
of all mirrors are listed in Table 1. Optical alignment of the IR beamline is difficult because its optical path is complex.

The M1 plane mirror is located 1.806 m from the light source. It has a central slot with a width of 3.0 mm to avoid overheating due to intense X-rays and UV light. After the IR beam is reflected horizontally by the extraction mirror, it is deflected by 90° and incident on the second plane mirror, M2, via the radiation protection wall. The distance between M2 and M1 is approximately 2.2 m. The IR beam, which is reflected by plance mirror M2, is redirected from a horizontal 90° angle to a vertical orientation before striking the first toroidal mirror, T1. Subsequently, T1 focusses the IR beam onto the CVD diamond window. To prevent multiple reflections, the window is designed with a wedge shape. It exhibits transparency in the infrared region and possesses an effective diameter of 22 mm. This arrangement effectively segregates the ultra-high vacuum (UHV) section of the beamline from the downstream high vacuum (HV) section.

Then, toroidal mirror T2 is placed behind the CVD diamond window with the same parameters as T1. It is used to correct the aberration of toroidal mirror T1, which has a compression ratio (object distance to image distance ratio) of 2.4. Therefore, the spot size of the far-IR region is compressed on the CVD diamond window, which improves the transmission efficiency of the far-IR region. This reduces the IR intensity loss owing to the effective size limitation of the diamond window.

An adjustable slit is placed at T2 focal point to limit the beam size and block stray light. The adjustment range of the slit is from 0 to 50 mm, and the adjustment accuracy is in the submillimeter range. Additionally, the front surface of the slit blade can be used as a visible-light target, and a CCD camera can be used to observe the position and shape of the focused spot of T2.

The plane mirror M4 is a switching mirror, which is used to control the direction of the IR beam. Furthermore, M4 is inserted into the optical path, and the IR beam is reflected to plane mirror M5b. A square spot is shaped by a pair of toroidal mirrors, T3b and T4b. The IR beam is focused and reflected by an optical matching system comprising M7b, T5b, and M8b. Finally, the IR beam is incident onto the FTIR spectrometer of the combined endstation BL05U.

When M4 is removed, the IR beam enters the IR experimental endstation BL06B. The role of the plane mirror M6a is to select the IR beam that enters the FTIR spectrometer or SNOM. Furthermore, T3a and T4a are the off-axis parabolic mirrors. The IR beam is collimated by T3a and incident onto the SNOM system. The IR beam is focused by T4a and incident onto the FTIR spectrometer of BL06B endstation.

2.4 Simulation

The photon flux of the main optical element is calculated using the SRW software, as shown in Fig. 2. It shows the photon flux of the SRIR source, M1, diamond window, and entrance of the FTIR spectrometer. Many factors are considered during the theoretical calculation, such as the dimensions of all optical components, the slot size of M1, 2%

Table 1 Parameters of the mirrors

Mirror	Type	Distance to source (mm)	Para. ($R_t \times R_s$) (mm²)	Coating	Dimensions ($L \times W$) (mm²)
M1	Flat	1.806	–	Al	140×70
M2	Flat	4.015	–	Au	150×200
T1	Toroidal	4.565	3794×1897	Au	290×120
Diamond	Edge(0.5°)	6.465	–	–	Φ25
T2	Toroidal	8.365	3794×1897	Au	290×120
M3	Flat	8.915	–	Au	260×110
M4	Flat	10.53	–	Au	110×130
M5a	Flat	13.33	–	Au	90×70
T3a	OAP	13.43	Focal length 500	Au	Φ50
M6a	Flat	13.68	–	Au	50×50
T4a	OAP	14.38	Focal length 200	Au	Φ50
M5b	Flat	15.33	–	Au	90×140
T3b	Toroidal	15.73	2409×2654	Au	90×140
M6b	Flat	21.03	-	Au	150×140
T4b	Toroidal	21.43	3431×2654	Au	150×140
M7b	Flat	24.925	–	Au	60×70
T5b	OAP	24.98	Focal length 750	Au	Φ60
M8b	Flat	25.18	–	Au	90×70
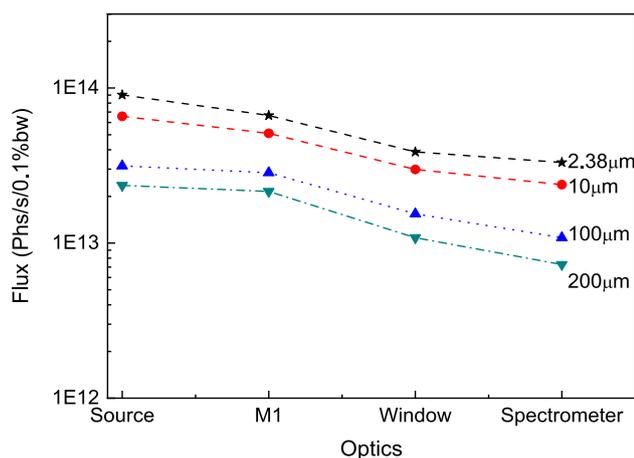
Fig. 2 Photon flux at the different optical elements, as calculated by SRW

loss per reflection, and 60% transmission efficiency of the CVD diamond window. The total losses have been considered along the entire IR beamline, and the photon flux of the entrance of FTIR spectrometer is predicted to be 3.3×10^{13} phs/s/0.1% B.W. @ 4200 cm^{-1} (2.38 μm, 300 mA) via theoretical calculation.

3 Experimental station

3.1 Key instrument

The main equipment of the BL06B endstation is a set of FTIR spectrometer (Bruker VERTEX 80v) and IR microscope (Hyperion 3000), as shown in Fig. 3. The high-resolution FTIR spectrometer is equipped with Si, KBr, and CaF$_2$ beam splitters, DTGS (with a KBr/PE window), MCT, InGaAs, and Si-bolometer detectors. It can cover a spectral

range of 10–10,000 cm^{-1}. Various accessories are available for the spectrometer, such as attenuated total reflection (ATR), automatic sample changer, combined transmission, and a specular reflection unit (angle of incidence 11°). A Bruker IR microscope is equipped with 4× visible objective, 15× and 36× IR/visible objectives. Furthermore, it is equipped with grazing angle incidence IR (GIR) objective, ATR objective, diamond anvil cell, mid-infrared polarizer, and a MCT detector (600–10000 cm^{-1}). The working distance of the 15× IR/visible objective lens is 24 mm. This method is suitable for in situ experimental cells. The SRIR source has a small size, high collimation, and high brightness. As a source for an IR microscope, it can easily focus on the optical diffraction limit. The signal-to-noise ratio (SNR) of SRIR is two to three orders of magnitude higher than that of globar source when the aperture size is below 15 μm × 15 μm using the IR microscope.

The IR SNOM is also purchased from Bruker with a model nano IR3, as shown in Fig. 4. The QCL laser is purchased together, and its wavenumber range is from 908 to 1668 cm^{-1}. There are two operating modes for SNOM device combined with a QCL laser. One of the modes is the atomic force microscopy IR (AFM-IR) mode, and the other mode is the SNOM mode with a MCT detector (600–10000 cm^{-1}). This technique enables the nano-analysis of samples using mid-IR spectroscopy with resolutions beyond the diffraction limit [21, 22]. AFM-IR spectroscopy is a powerful technique, and it uses AFM tip to directly detect the samples. A thermal expansion effect is generated due to the IR absorption of the sample when the IR laser is focused on the sample, causing the tip to oscillate in the AFM cantilever. The oscillation amplitude of the AFM cantilever is proportional to the IR absorption of the sample. The AFM-IR technology exhibits broad application prospects, especially for samples with high thermal expansion coefficients, such as soft materials and biological samples. The spatial resolution of

Fig. 3 (Color online) IR spectrometer and microscope (VERTEX 80v and Hyperion 3000, Bruker)

Fig. 4 (Color online) Scan near-field optical microscope (NanoIR3, Bruker)

the experimental measurements is related to the radius of curvature of the AFM tip, which is better than 50 nm. Therefore, the AFM-IR technique is used to identify the chemical composition of a sample at the nanoscale, and it is mainly used for spectral measurements at specified positions and imaging at fixed wavenumbers.

SNOM technology has played an increasingly important role in the investigation of nanoscale properties and structures of various materials. The basic principle of s-SNOM is that an illuminated AFM tip forms an enhanced light field that can be used as a scattering source. The near field is changed by a nearby sample, and the optical properties of the sample are obtained. The spatial resolution is better than 50 nm and is independent of the wavelength of the incident light. Given that the scattered near-field signal from the AFM tip is extremely weak, the effective extraction of near-field information is a key issue.

3.2 In situ accessory

Some in situ sample cells are available for IR spectrometer and microscope:

1. Oxford low-temperature instrument: This is a dry, compact cryostat providing optical access to a temperature-controlled sample in vacuum. The temperature is varied from room temperature to 4 K.
2. High-temperature high-pressure (HTHP) cell: The sample is placed in the central sample post-heater mount. The experimental measurement is from room temperature to 800 °C (under vacuum conditions). The pressure is varied from vacuum (0.003 Torr) to 1000 psi for all the in situ reaction studies.
3. HTHP Diffuse Reflectance Accessory: The solid powder samples are placed in a heatable sampling cup within a controllable chamber. The experiment of diffuse reflectance is measured from room temperature to 800 °C, and the pressure ranges from vacuum (0.001 Torr) to 500 psi.
4. Linkam Temperature Controlled stage (THMS600) is equipped for the IR microscope with a minimum temperature of –196 °C and maximum temperature of 600 °C.

3.3 Experimental methods

1. IR spectroscopy: transmission, reflection, ATR, and diffuse reflection. The chemical composition and structural information of the samples are obtained using these methods.
2. IR microspectroscopy: transmission, reflection, ATR, and GIR. The spatial distribution and components of

the sample are obtained, and the spatial resolution approaches the optical diffraction limit.
3. Nano-IR spectroscopy and imaging: AFM-IR and SNOM technologies have been developed using SNOM devices combined with a QCL laser. In both methods, the experimental spatial resolution is better than 50 nm.

4 First commissioning results

At the end of 2020, some performance parameters of BL06B station were measured, including the spectral range, spectral resolution, focused spot size (IR microscope), and photon flux at the entrance of the spectrometer.

After aligning the optical path of the SRIR beamline, the photon flux was measured at the entrance of the spectrometer. The parallel SRIR beam passed through an optical filter (NB-2380-052 nm, Spectrogon Corporation) and was then focused by a parabolic mirror into a calibrated Si diode (G12183-030 K, Hamamatsu, Inc.). Finally, photocurrent was measured using a picoammeter. The photon flux can be derived from a series of formulas. The photon flux was 3.2×10^{13} phs/s/0.1% B.W. @4200 cm^{-1} for a 300-mA injection current. The details of the measurement and calculation methods are provided in Ref. [2]. The photon flux (the entrance of the FTIR spectrometer) was predicted to be 3.3×10^{13} phs/s/0.1% B.W. at 4200 cm^{-1} (300 mA) via theoretical calculation, as shown in Fig. 2. The aforementioned results show that the experimental measurements are highly consistent with the photon flux calculated using the SRW software.

The focused spot size of IR microscope is completed by a pinhole with 5 μm diameter, the SRIR source and a pair of 36× objectives. The MCT detector is also used in the spectral range of 600–10000 cm^{-1}. Two-dimensional mapping of the SRIR spot size was performed using the OPUS software. The experimental parameters are the following: spectral resolution 4 cm^{-1} and 16 scans. The step size is 2 μm in the *X* and *Y* direction. Three-dimensional intensity distribution of SRIR beam is shown in Fig. 5 at 1000 cm^{-1}. Furthermore, the intensity distribution of the focused spot is extracted along the horizontal direction (*H*) and vertical direction (*V*) at 1000 cm^{-1}. The corresponding full width value is 24 μm. According to the formula $1.22\lambda/NA$ (NA = 0.5), theoretical value of optical diffraction limit is 24.4 μm. The experimental measurement was very close to the theoretical value. The SRIR beam allowed more light to enter smaller pinholes. However, it is not possible to obtain the above results using global sources. The experimental results show that the high collimated nature and considerable brightness of the SRIR beam are advantageous for IR microspectroscopy.

The spectral resolution of the IR spectrometer was measured when the SRIR light source was introduced into the
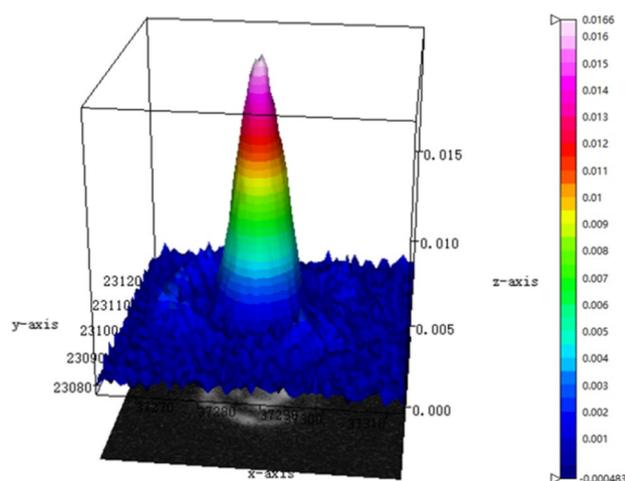
Fig. 5 (Color online) Three-dimensional intensity distribution is obtained using a pinhole (diameter of 5 μm)

Table 2 Performance of the IR microspectroscopy endstation

Spectral range	10–10,000 cm^{-1} (Spectrometer), 600–10,000 cm^{-1} (Microscope)
Spectral resolution	0.1 cm^{-1}
Photon flux (entrance of the spectrometer)	3.2×10^{13} phs/s/0.1% B.W. @ 4200 cm^{-1} @300 mA
Focused spot size	~24 μm@1000 cm^{-1} (Full Width)

Bruker VERTEX 80v spectrometer. A KBr beam splitter and a MCT detector were used for the performance measurements. CO gas was sealed in a gas pool as the test sample. The absorbance spectrum of the CO gas was obtained in the mid-infrared region. The FWHM of absorption peak was 0.07 cm^{-1}.

The performance parameters of the IR beamline endstation were obtained and are listed in Table 2. The spectral range covers 10–10,000 cm^{-1} for the IR spectrometer, the spectral resolution is better than 0.1 cm^{-1}. The photon flux was 3.2×10^{13} phs/s/0.1% B.W. @ 4200 cm^{-1} @ 300 mA at the entrance of the spectrometer. For the IR microscope, the spectral range is from 600 to 10,000 cm^{-1} as the detector is restricted. The focused spot diameter is 24 μm at 1000 cm^{-1} by the 36× objective, which reaches diffraction-limited spatial resolution.

5 First user achievements

SRIR microspectroscopy is a powerful technique for examining IR spectra and mapping samples with a diffraction-limited spatial resolution. The BL06B endstation has been widely used in various research fields.

In chemistry science, a superfast pathway for zeolite was established with nano-channels by J. M. Yuan et al. [23]. The adsorption configurations and diffusion processes of different long-chain alkanes in different zeolite channels were directly measured via SRIR microspectroscopy. These results provide direct experimental evidence for theoretical simulations. Based on the adsorption rate diffusion experiments, it was determined that the diffusion trend and pore size of short- and long-chain alkanes showed completely opposite results for zeolites. Furthermore, SRIR experiments verified the deformation differences between long-chain molecules with different pore sizes. Additionally, the acquisition of in situ high-temperature transmission IR microscopic mapping was conducted by Mingbin Gao et al. [24]. The ratio of low-carbon to long-chain olefins in different zeolite topologies was directly captured via SRIR mapping during the methanol-to-olefin reaction. Moreover, a quantitative model of shape-selective catalysis is proposed in this study, and its mechanism can be explained during the catalytic process of the zeolite framework using SRIR information. An in situ high-temperature FTIR experiment was completed by Hu et al. [25]. Isolated co-motifs were incorporated into the MFI zeolite framework using pure silicon. The position, structure, and microenvironment of the Co atoms are revealed by their unique catalytic effect on the PDH reaction. The in situ high-temperature FTIR experiment was completed at the BL06B endstation of the Shanghai Light Source. The results demonstrate that the H element of the active center $\{(\equiv SiO)_2Co(HO-Si\equiv)_2\}$ is involved in the dehydrogenation process, and the proposed reaction mechanism is verified.

In materials science, silk protein ion elastomers were achieved through a casting solution and high-humidity induction technology by Gao et al. [26]. SRIR microspectroscopy was used to characterize the ion elastomers of the silk fibroin. The secondary structure of the protein was determined by integrating the characteristic peak (amide I) of silk fibroin. After three days of high-humidity treatment, the β-sheet structure was approximately only 20%. This method effectively solves the material-hardening problem. High-humidity treatment, as a mild and controllable induction method, significantly improves the tensile strength of silk protein ion elastomers. Zhang et al. examined the structure and mechanical stability of porous MOF materials using in situ high-pressure SRIR microspectroscopy and a diamond pressure machine [27]. Furthermore, MOF with high mechanical stabilities have been developed for industrial applications. The source of the mechanical stability of porous materials has been clarified, and the controllable synthesis of MOF material with specific mechanical stability has been proposed.

In environmental science, functional group quantification analysis of aquatic green algae was studied by Zhiqiang Shi

et al. [28]. The toxic effects of Cd on Cosmarium sp. cells were characterized in vivo using SRIR microspectroscopy. The mapping and functional group quantification of biological macromolecules were conducted within a single algal cell. The results showed that the biosynthesis of biological macromolecules, such as carbohydrates, proteins, and lipids, in algal cells, is inhibited by heavy metals. Additionally, correlation analysis and principal component analysis show a good correlation between ν (C–OH)/Amide II and biochemical parameters of algae cells. These results indicate that carbohydrate changes in algal cells can serve as biomarkers of the toxic effects of heavy metals on single-cell microalgae.

In biomedical science, BL06B endstation was used to examine the SRIR spectra and component distributions of pathological tissues by Shanshan Guo et al. [29]. The SRIR spectra effectively revealed the lipid, protein, and nucleic acid characteristics of breast tumors and normal tissues. These results complemented the X-ray phase-sensitive microtomography (XPCT) data. It recognized tumor markers in complex biomolecules. The average infrared spectra of breast tumors at different stages showed differences in the characteristic peaks of lipids, proteins, and nucleic acids. SRIR mapping and spectral technologies are effective tools for identifying cancerous tissues. Single cells from the pancreatic islets of mice were measured using SRIR spectra as described by Wang et al. [30]. The original absorption spectra of single cells were obtained (200 cells). Pancreatic islet cells were subdivided into five main groups, and their proportions were quantitatively determined using PCA and other analytical methods. These results demonstrate that infrared spectra of single cells are valuable complementary techniques for describing cellular heterogeneity within pancreatic islets.

6 Summary and conclusion

The IR beamline BL06B of the SSRF was introduced in this study. Furthermore, the optical layout was described. Some performance parameters of the BL06B endstation were measured, including the focused spot size (IR microscope), spectral resolution, and photon flux at the entrance of the spectrometer. The results showed that the photon flux is in good agreement with the theoretical calculations. The focused spot of the SRIR microscope realized a diffraction-limited spatial resolution. With high spatial resolution, several SRIR applications have been completed by users, and primary user achievements have been described. Using IR SNOM, this technique can realize the nano-analysis of samples by mid-IR spectroscopy with a spatial resolution of tens of nanometers. The IR endstation can be used for application research in a wide range of fields, including materials, chemistry, biology, geophysics, and pharmacology.

Declarations

Conflict of interest The authors declare that they have no competing interests.

References

1. T. Ji, Y.J. Tong, H.C. Zhu et al., The status of the first infrared beamline at Shanghai synchrotron radiation facility. Nucl. Instrum. Meth. A **788**, 116–121 (2015). https://doi.org/10.1016/j.nima.2015.03.080

2. Z.Y. Zhang, M. Chen, Y.J. Tong et al., Performance of the infrared microspectroscopy station at SSRF. Infrared. Phys. Technol. **67**, 521–5250 (2014). https://doi.org/10.1016/j.infrared.2014.09.015

3. Y.D. Wang, X.L. Li, J. Hu et al., Synchrotron infrared spectral regions as signatures for foodborne bacterial typing. Nucl. Sci. Tech. **30**, 25 (2019). https://doi.org/10.1007/s41365-019-0554-x

4. J.F. Liu, S. Wang, R.J. Yang et al., Bio-inspired graphene oxide-amino acid cross-linked framework membrane trigger high water permeance and high metal ions rejection. J. Membr. Sci. **659**, 120745 (2022). https://doi.org/10.1016/j.memsci.2022.120745

5. Y. Wang, J. Ren, Z.C. Lv et al., Direct functionalization of natural silks through continuous force-reeling technique. Chem. Eng. J. **435**, 134901 (2022). https://doi.org/10.1016/j.cej.2022.134901

6. J. Qian, X. Gao, Y.D. Wang et al., Synchrotron infrared microspectroscopy for stem cell research. Int. J. Mol. Sci. **23**, 9878 (2022). https://doi.org/10.3390/ijms23179878

7. W.W. Zhang, S. Yang, R.X. Peng et al., Hierarchically non-uniform structures determine the hydro-actuated bending deformation of camel hair. Cell Rep. Phys. Sci. **3**, 100793 (2022). https://doi.org/10.1016/j.xcrp.2022.100793

8. S.S. Guo, G.X. Wei, W.Q. Chen et al., Fast and deep diagnosis using blood-based ATR-FTIR spectroscopy for digestive tract cancers. Biomolecules **12**, 1815 (2022). https://doi.org/10.3390/biom12121815

9. L.L. Wang, H.Y. Du, H.C. Xu et al., Insights into phenanthrene attenuation by hydroxyl radicals from reduced iron-bearing mineral oxygenation. J. Hazard. Mater. **439**, 129658 (2022). https://doi.org/10.1016/j.jhazmat.2022.129658

10. J. Qian, Y.D. Wang, X.L. Li et al., Hydrogel microenvironment contributes to chemical-induced differentiation of mesenchymal stem cells: single-cell infrared microspectroscopy characterization. Anal. Bioanal. Chem. **415**, 3305 (2023). https://doi.org/10.1007/s00216-023-04746-z

11. T.T. Zuo, M. Xie, M.L. Yan et al., In situ analysis of acupuncture protecting dopaminergic neurons from lipid peroxidative damage

in mice of Parkinson's disease. Cell Proliferat. **55**, e13213 (2022). https://doi.org/10.1111/cpr.13213

12. C.X. Huang, J. Xu, J. Li et al., Hydrogen peroxide responsive covalent cyclodextrin framework for targeted therapy of inflammatory bowel disease. Carbohydr. Polym. **285**, 119252 (2022). https://doi.org/10.1016/j.carbpol.2022.119252

13. C. Chen, Q. Shi, M.Z. Li et al., Engineering an enthesis-like graft for rotator cuff repair: An approach to fabricate highly biomimetic scaffold capable of zone-specifically releasing stem cell differentiation inducers. Bioact. Mater. **16**, 451 (2022). https://doi.org/10.1016/j.bioactmat.2021.12.021

14. I. Yousef, S. Lefrancois, T. Moreno et al., Simulation and design of an infrared beamline for SESAME (Synchrotron-light for Experimental Science and Applications in the Middle East). Nucl. Instrum. Methods Phys. Res. A **673**, 73 (2012). https://doi.org/10.1016/j.nima.2011.12.012

15. X.J. Zhou, H.C. Zhu, J.J. Zhong et al., New status of the infrared beamlines at SSRF. Nucl. Sci. Tech. **30**, 182 (2019). https://doi.org/10.1007/s41365-019-0696-x

16. D. Creagh, J. Mckinlay, P. Dumas, The design of the infrared beamline at the Australian synchrotron. Vib. Spectrosc. **41**, 213 (2006). https://doi.org/10.1016/j.vibspec.2006.02.009

17. P. Roy, M. Rouzieres, Z.M. Qi et al., The AILES infrared beamline on the third generation synchrotron radiation facility SOLEIL. Infrared Phys. Technol. **49**, 139 (2006). https://doi.org/10.1016/j.infrared.2006.01.015

18. H.J. Xu, Z.T. Zhao, Current status and progresses of SSRF project. Nucl. Sci. Tech. **19**, 1 (2008). https://doi.org/10.1016/S1001-8042(08)60013-5

19. J.H. He, Z.T. Zhao, Shanghai synchrotron radiation facility. Natl. Sci. Rew. **1**, 171 (2014). https://doi.org/10.1093/nsr/nwt039

20. R.A. Bosch, Computed flux and brightness of infrared edge and synchrotron radiation. Nucl. Instrum. Methods A **454**, 497 (2000). https://doi.org/10.1016/S0168-9002(00)00476-9

21. D. Perez-Guaita, K. Kochan, M. Batty et al., Multispectral atomic force microscopy-infrared nano-imaging of malaria infected red blood cells. Anal. Chem. **90**, 3140 (2018). https://doi.org/10.1021/acs.analchem.7b04318

22. G.B. Dai, Z.B. Yang, G.S. Geng et al., Signal detection techiniques for scattering-type scanning near-field optical microscopy. Appl. Spectrosc. Rev. **53**, 806 (2018). https://doi.org/10.1080/05704928.2018.1443275

23. J.M. Yuan, M.B. Gao, Z.Q. Liu et al., Hyperloop-like diffusion of long-chainmolecules under confinement. Nat. Commun. **14**, 1735 (2023). https://doi.org/10.1038/s41467-023-37455-3

24. M.B. Gao, H. Li, J.Y. Yu et al., Quantitative principle of shape-selective catalysis for a rational screening of zeolites for methanol-to-hydrocarbons. AIChE J. **68**, e17881 (2022). https://doi.org/10.1002/aic.17881

25. Z.P. Hu, G.Q. Qin, J.F. Han et al., Atomic insight into the local structure and microenvironment of isolated co-motifs in MFI zeolite frameworks for propane dehydrogenation. J. Am. Chem. Soc. **144**, 12127 (2022). https://doi.org/10.1021/jacs.2c02636

26. L.T. Cao, C. Ye, H. Zhang et al., An artificial motion and tactile receptor constructed by hyperelastic double physically cross-linked silk fibroin ionoelastomer. Adv. Funct. Mater. **33**, 2301404 (2023). https://doi.org/10.1002/adfm.202301404

27. Z.Y. Zhang, G.X. Qin, X.M. Li et al., Enhanced mechanical stability and proton conductivity performance from the dense Mn(II)-Metal-Organic framework to porous Mn(II)−Fe(III)-Metal−Organic framework. Inorg. Chem. **61**, 15166 (2022). https://doi.org/10.1021/acs.inorgchem.2c02357

28. Z.Q. Shi, M.J. Guo, H.Y. Du et al., Investigation of cytotoxic cadmium in aquatic green algae by synchrotron radiation-based Fourier transform infrared spectroscopy: Role of dissolved organic matter. Sci. Total. Environ. **870**, 161870 (2023). https://doi.org/10.1016/j.scitotenv.2023.161870

29. S.S. Guo, J.S. Xiu, L.N. Kong et al., Micro-tomographic and infrared spectral data mining for breast cancer diagnosis. Opt. Laser. Eng. **160**, 107305 (2023). https://doi.org/10.1016/j.optlaseng.2022.107305

30. Y.D. Wang, Y. Gao, X.L. Li et al., Single-cell infrared phenomics identifies cell heterogeneity of individual pancreatic islets in mouse model. Anal. Chim. Acta **1258**, 341185 (2023). https://doi.org/10.1016/j.aca.2023.341185